Journal of Zhejiang University-SCIENCE A (Applied Physics & Engineering) 2025 26(5):438-455
www.jzus.zju.edu.cn; www.springer.com/journal/11582
E-mail: jzus_a@zju.edu.cn

Research Article

https://doi.org/10.1631/jzus.A2400039

Aerodynamics and countermeasures of train-tail swaying inside single-line tunnels

Yadong SONG[1], Yanpeng ZOU[2], Yuan YAO[1,3]✉, Ting QIN[1], Longjiang SHEN[3]

[1]*State Key Laboratory of Rail Transit Vehicle System, Southwest Jiaotong University, Chengdu 610031, China*
[2]*Foundation Service Department of CRRC Changke Co., Ltd., Changchun 130062, China*
[3]*State Key Laboratory of Heavy-duty and Express High-power Electric Locomotive, CRRC Zhuzhou Electric Locomotive Co., Ltd., Zhuzhou 412000, China*

Abstract: In recent years, train-tail swaying of 160 km/h electric multiple units (EMUs) inside single-line tunnels has been heavily researched, because the issue needs to be solved urgently. In this paper, a co-simulation model of vortex-induced vibration (VIV) of the tail car body is established, and the aerodynamics of train-tail swaying is studied. The simulation results were confirmed through a field test of operating EMUs. Furthermore, the influence mechanism of train-tail swaying on the wake flow field is studied in detail through a wind-tunnel experiment and a simulation of a reduced-scaled train model. The results demonstrate that the aerodynamic force frequency (i.e., vortex-induced frequency) of the train tail increases linearly with train speed. When the train runs at 130 km/h, with a small amplitude of train-tail swaying (within 10 mm), the vortex-induced frequency is 1.7 Hz, which primarily depends on the nose shape of the train tail. After the tail car body nose is extended, the vortex-induced frequency is decreased. As the swaying amplitude of the train tail increases (exceeding 25 mm), the separation point of the high-intensity vortex in the train wake shifts downstream to the nose tip, and the vortex-induced frequency shifts from 1.7 Hz to the nearby car body hunting (i.e., the primary hunting) frequency of 1.3 Hz, which leads to the frequency-locking phenomenon of VIV, and the resonance intensifies train-tail swaying. For the motor vehicle of the train tail, optimization of the yaw damper to improve its primary hunting stability can effectively alleviate train-tail swaying inside single-line tunnels. Optimization of the tail car body nose shape reduces the amplitude of the vortex-induced force, thereby weakening the aerodynamic effect and solving the problem of train-tail swaying inside the single-line tunnels.

Key words: Train-tail swaying; Vortex-induced vibration (VIV); Wake flow field; Train aerodynamics; Vehicle dynamics

1 Introduction

1.1 Engineering background

In China, since power-concentrated electric multiple units (EMUs) with a speed level of 160 km/h were put into operation in Jan. 2019, some of the vehicles have exhibited lateral dynamics issues. In addition to the lack of hunting stability on local lines (Shi et al., 2020; Sun et al., 2021; Li W et al., 2022), there is a discrepancy in the lateral ride index between the two ends of the locomotive (Li et al., 2023a, 2023b), and the deterioration of lateral ride comfort caused by continuous swaying of the train tail inside single-line tunnels is particularly serious (Yao et al., 2021). When EMUs pass through a single-line tunnel, the constant swaying of the tail car body is obvious, which has attracted the attention of relevant railway departments. As the phenomenon only occurs inside tunnels, it has been suggested that it is not associated with the track irregularities or self-induced hunting motion, but is caused by the external aerodynamics of the train wake.

According to our on-track tests and simulation analysis of actual operating EMUs, train-tail swaying only occurs within a specific speed range of 120–130 km/h, and the phenomenon disappears as train speed increases. Therefore, it is not a result of negative damping vibration; the aerodynamic effects of galloping and flutter are thus excluded, and vortex-induced

✉ Yuan YAO, yyuan8848@163.com
Yadong SONG, https://orcid.org/0000-0002-4809-7329
Yuan YAO, https://orcid.org/0000-0003-2279-7463

Received Jan. 19, 2024; Revision accepted Apr. 25, 2024; Crosschecked Mar. 3, 2025

vibration (VIV) is obviously more reasonable as a cause. To address this practical problem, it is necessary to clarify the relevant mechanism and propose corresponding solutions.

1.2 Review of related research

Train swaying inside tunnels was initially discovered in the 1990s in Japan. The car body lateral swaying was most noticeable on the Shinkansen, and it gradually increased from the front vehicle to the rear vehicle of the train (Fujimoto et al., 1993). The swaying of train tails inside tunnels has been the subject of numerous studies. Takai (1990) first proposed that the aerodynamic load inside tunnels was the primary cause and that track disturbance had little impact. Earlier studies (Suzuki, 2000, 2001, 2004) by the Railway Technical Research Institute (RTRI) in Japan also showed that a propagation pressure disturbance (PPD) was generated alongside the car body in the tunnel, and was strong enough to negatively impact ride comfort. Diedrichs et al. (2007, 2008) studied the aerodynamic response of the tail car bodies of the Japanese S300 and German ICE2 trains inside tunnels using large eddy simulation (LES). They found that the flow separation caused the vibration of the tail car body, leading to a linear increase in pressure disturbance from the nose to around 150–200 m downstream. Based on the car body pressure data measured inside tunnels, Tanifuji et al. (2008) developed a mathematical model to study the ride comfort of trains under an aerodynamic load in tunnels.

As the running speed of railway vehicles increases, it inevitably leads to the deterioration of aerodynamic performance. Over the past decade, computational fluid dynamics (CFD) and wind-tunnel tests have advanced rapidly, and many scholars have conducted more in-depth research on the aerodynamic performance of railway vehicles. Choi and Kim (2014) used CFD simulation to study the effect of train-nose length and tunnel cross-sectional area on a car body's aerodynamic drag in tunnels. Niu et al. (2016, 2017, 2018) studied the aerodynamic force of a CRH380A train under different operating conditions through numerical simulation and wind-tunnel tests on a reduced-scale train model. Zeng et al. (2014, 2018) analyzed the car body hunting performance of a high-speed train under constant aerodynamic load by numerical simulation. Pan et al. (2018) studied the wake vortex structure of a high-speed train by vortex identification methods, and found that powerful vortices with high vorticity magnitude mostly appeared near the tail car. Through numerical modeling, Du et al. (2022) explored how the number of cars affected both the aerodynamic pressure and micropressure waves in a tunnel. Wang et al. (2022) studied the effect of wheel-rail contact characteristics and aerodynamic forces on car body hunting performance. Li et al. (2021, 2023) conducted extensive research on the aerodynamic resistance during train operation, and used a vortex generator (VG) to reduce the tail car body aerodynamic resistance in an ICE2 high-speed train.

VIV is a classic fluid–structure interaction (FSI) phenomenon, which is caused by the vibration of fluid coupled to the elastic system (Williamson and Govardhan, 2004; Han et al., 2023). At present, the research on VIV theory is mainly focused on structures with slender appearance such as marine pipelines and large-span bridges, and much progress has been made (Yu et al., 2023; Zhang et al., 2023; Zhao et al., 2023). VIV occurs when the vortex-induced frequency approaches a certain natural frequency of the structure, and the frequency of vortex-induced force is "locked" on that natural frequency at the same time (Liu et al., 2023). The significant difference between a train and other ground vehicles is that a train has a large slenderness ratio in terms of fluid mechanics. The flow of air surrounding the train is also distinct from that of airplanes, owing to its interaction with the ground. The flow field around a train is basically a 3D turbulent flow because of its geometric features and running speed (Khier et al., 2000). Due to the imperfections of vibration theory, it is helpful to study VIV through wind-tunnel tests (Zhou and Ge, 2008). Bell et al. (2014, 2015, 2016a, 2016b) analyzed the slipstream and wake of an ICE3 high-speed train with a 1/10-scale wind-tunnel experiment. Hemida and Krajnović (2008, 2009) discovered that there was a certain relationship between car body vibration and the vortex-induced frequency of a train's wake.

1.3 Motivation and contribution of this study

The main questions that motivated this study are as follows:

1. How do aerodynamic forces cause the tail of 160 km/h EMUs to continuously sway inside single-line tunnels, leading to a deterioration in ride comfort?

2. What is the magnitude and corresponding frequency of the aerodynamic force that causes train-tail swaying inside single-line tunnels, and what is the vibration frequency of train-tail swaying?

3. What effective measures can be taken to alleviate the swaying phenomenon of the EMU tail inside single-line tunnels?

The scope of this study draws attention to a relatively new topic, namely the car body vibration induced by aerodynamics that ultimately affects ride comfort through vehicle dynamics.

During actual train operation, the swaying of the tail car body interacts with the wake flow field, and the aerodynamic force generated by the train wake is unsteady. Therefore, it was necessary for us to carry out a transient analysis of FSI. As far as we know, the majority of previous studies applied the calculated aerodynamic force as the constant excitation to the car body, while a minority focused on assessing car body vibration with regard to FSI. Regrettably, little research has been done on how VIV affects a vehicle system's aerodynamic performance. These were additional challenges for us in carrying out this research.

In this paper, we establish a co-simulation model for the VIV of a 160 km/h EMU tail in a single-track tunnel, and experimentally clarify the mechanism of train-tail swaying caused by VIV. Finally, we propose effective measures to alleviate the problem of train-tail swaying in single-line tunnels by optimizing vehicle suspension and tail nose shape.

2 Methodology

2.1 Technical route

To study train-tail swaying of 160 km/h EMUs in a single-line tunnel, we adopted a combination of simulation and experimental methods, and the specific technical route is shown in Fig. 1. The key of the simulation method was to establish the fluid–structure coupled simulation platform, which analyzed the flow characteristics of the train wake and the dynamic performance of the tail vehicle. The key aspects of the experimental method were constructing a wind-tunnel test bench for a 1/25-scale train model, and conducting on-track tests of the actual running train. We then

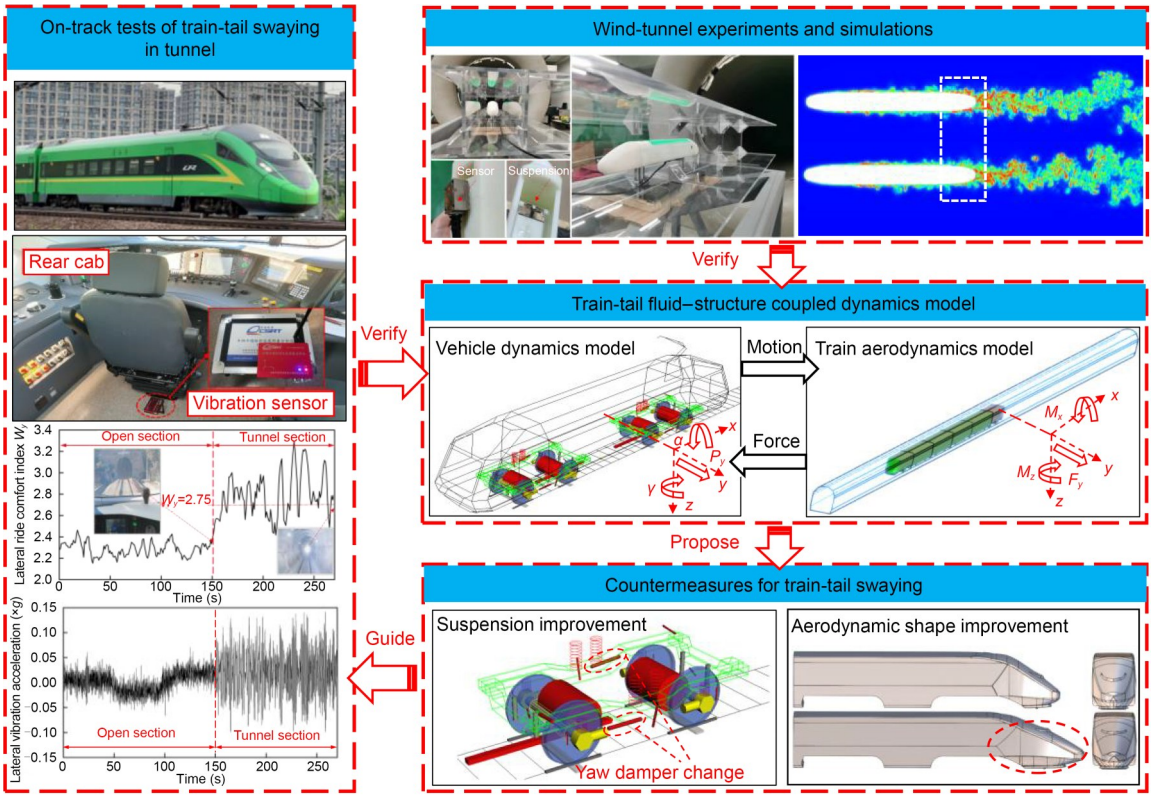

Fig. 1 Research flow of this study. The variables M_x, M_z, and F_y are described in Section 3.2, and the variables P_y, α, and γ are described in Section 4.2

verified the simulation results with experiments. Finally, through simulation analysis, we were able to determine the effective measures to alleviate train-tail swaying inside tunnels.

There are two main methods of fluid–structure coupled calculation: the partitioned method and the monolithic method. We used the partitioned method, which solves the flow field and dynamics separately. The simulation of train-tail swaying in the tunnel was based on the vehicle dynamics model and train aerodynamics model shown in Fig. 2a, and the specific coupled calculation flow is shown in Fig. 2b. The *x*-axis represents the direction along the rail, the *z*-axis represents the direction perpendicular to the ground, and the *y*-axis represents the transverse direction. The specific calculation process was illustrated in detail in our recent study (Song et al., 2023). In addition, the consistent time-step Δt and the number of steps n employed in the following transient simulation were 0.05 ms and 800×10^3, respectively.

2.2 Vehicle dynamics sub-model

The dynamics model of the 160 km/h EMU tail motor vehicle was developed in the SIMULIA Simpack 2020. The whole vehicle multi-body system has 25 rigid bodies and 90 degrees of freedom. For the vehicle suspension system, the secondary suspension consists of a yaw damper, secondary lateral and vertical damper, and flex-coil springs; the primary suspension consists of an axle box spring, a rotating arm, and primary vertical dampers, as shown in Fig. 3. Moreover, all dampers are based on the Maxwell model; the wheel/rail functions are constructed with the CN60 rail and JM3 wheel profiles; the track irregularity is based on the irregularity described in Li et al. (2014). Our other related studies (Li G et al., 2022; Song et al., 2023) listed the main dynamic parameters and structures of the motor vehicle, and also described how we confirmed the accuracy and reliability of the Simpack model.

2.3 Train aerodynamics sub-model

The CFD model of the train aerodynamics simulation inside a tunnel was established in the SIMULIA XFlow 2021x, and was based on the particle method. We used a 160 km/h EMU for numerical simulation (Fig. 4). The train model is simplified according to the CEN standard (CEN, 2019, 2022), and the shape of the single-line tunnel is based on the standard of GB 146.2-2020 (NRA, 2020). The train height *H*, also known as the characteristic length in train aerodynamics, is 4.0 m at 1 : 1 scale.

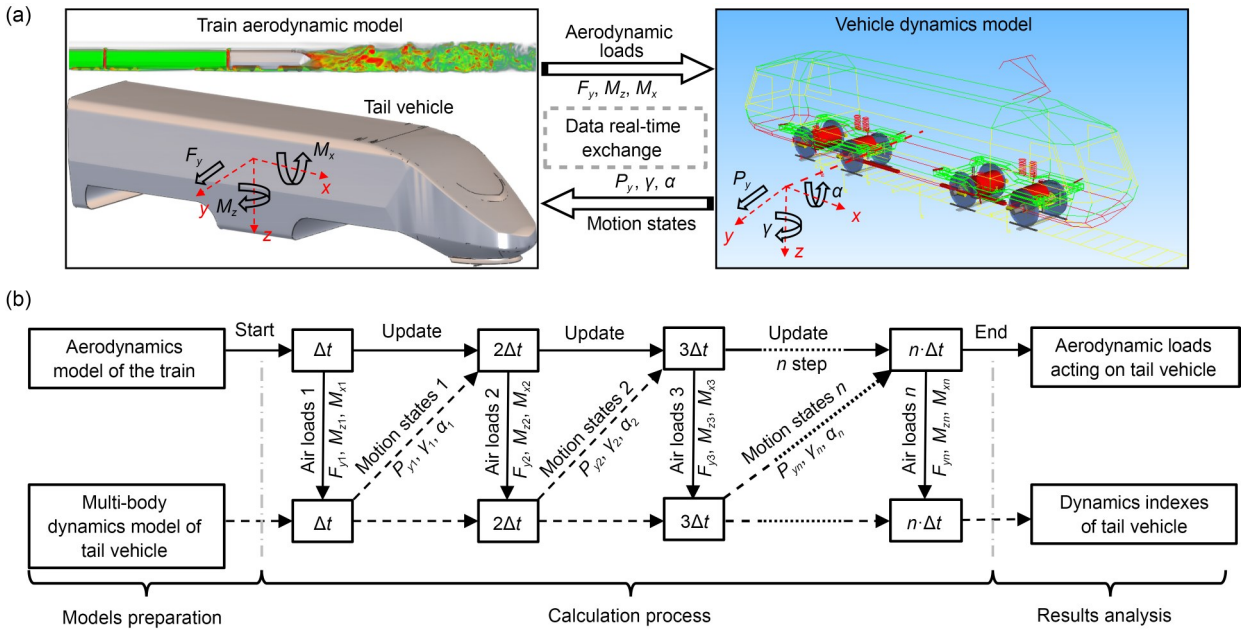

Fig. 2 Fluid–structure coupled simulation for train-tail vibration: (a) model; (b) flowchart. The variables M_x, M_z, and F_y are described in Section 3.2; the variables P_y, α, and γ are described in Section 4.2; M_{xn}, M_{zn}, F_{yn}, P_{yn}, α_n, and γ_n represent the states of the first six variables at step n, respectively

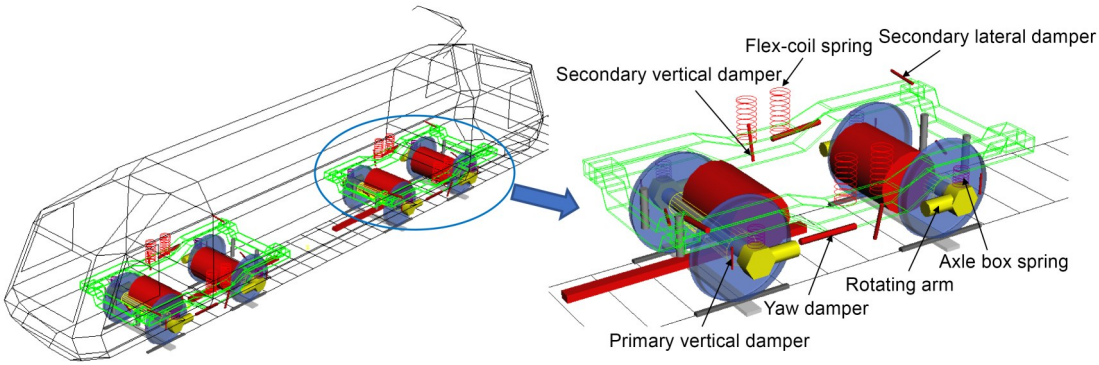

Fig. 3 Dynamics model of the motor vehicle

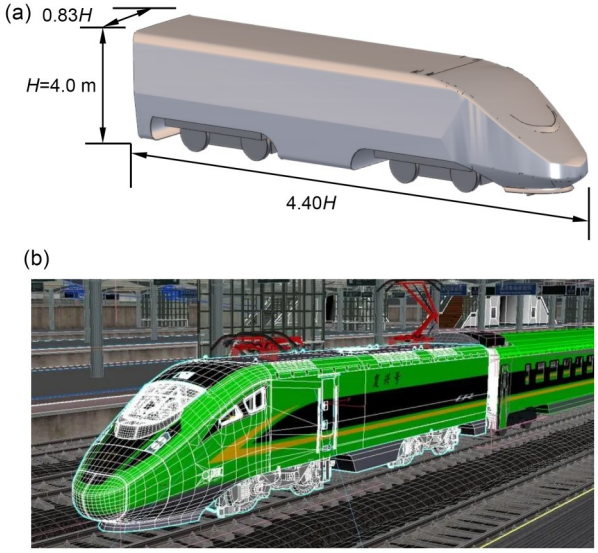

Fig. 4 EMU model of 160 km/h in this study: (a) train model employed in numerical simulation; (b) actual train

The aerodynamics model of a train running inside a single-line tunnel is illustrated in Fig. 5. The train is located at a distance of 20H from the tunnel inlet and 45H from the tunnel outlet, which prevents the influence of boundary conditions on the flow field around the train referring to the EN 14067-6 standard (CEN, 2022). The tunnel inlet is defined as the velocity inlet boundary condition, and the inlet velocity U is the train speed along the x-axis. The tunnel outlet is defined as the pressure outlet boundary condition, with a reference pressure of 0 Pa. The train's surface and the tunnel's inner wall are defined as the non-equilibrium enhanced wall-functions in XFlow (SIMULIA Inc., 2021). The Reynolds number Re in this simulation is about 8.1×10^6, and the formula is as follows:

$$Re=\rho UH/\mu. \tag{1}$$

Considering that the on-track tests in Section 4 were conducted in an area with high elevation, the air density ρ is set to 1.01 kg/m^3, and the air viscosity parameter μ is set to 17.9×10^{-6} Pa·s. In addition, the train speed U is 36 m/s (130 km/h) in the tunnel.

In the numerical simulation, the calculated particle is the octree lattice structure of the D3Q27 organization constructed by XFlow according to the given geometry (SIMULIA Inc., 2021). The calculated particle distribution of the computational domain is illustrated in Fig. S1 of the Electronic Supplementary Materials (ESM), and the accuracy of the train aerodynamics model has been proved in our recent research (Song et al., 2023), which is not illustrated here.

3 Simulation

3.1 Calculated conditions

On an actual railway line, the track operation environment in tunnels is relatively poor and maintenance is difficult. In order to simulate the coupling vibration caused by the EMU tail swaying in a single-line tunnel, three kinds of line conditions (Cond) are set in this section, corresponding to three different scales of track irregularity: Cond 1: smooth line, with no track irregularity; Cond 2: normal line, with track irregularity; Cond 3: poor line, with the amplitude of track lateral irregularity doubled. The track irregularity is obtained by the high-speed track spectrum (Li et al., 2014). The lateral irregularity is shown in Fig. S2 of the ESM. In addition, the simulation time is set to 40 s, the vehicle speed is 130 km/h, and other parameters are as introduced in Section 2.

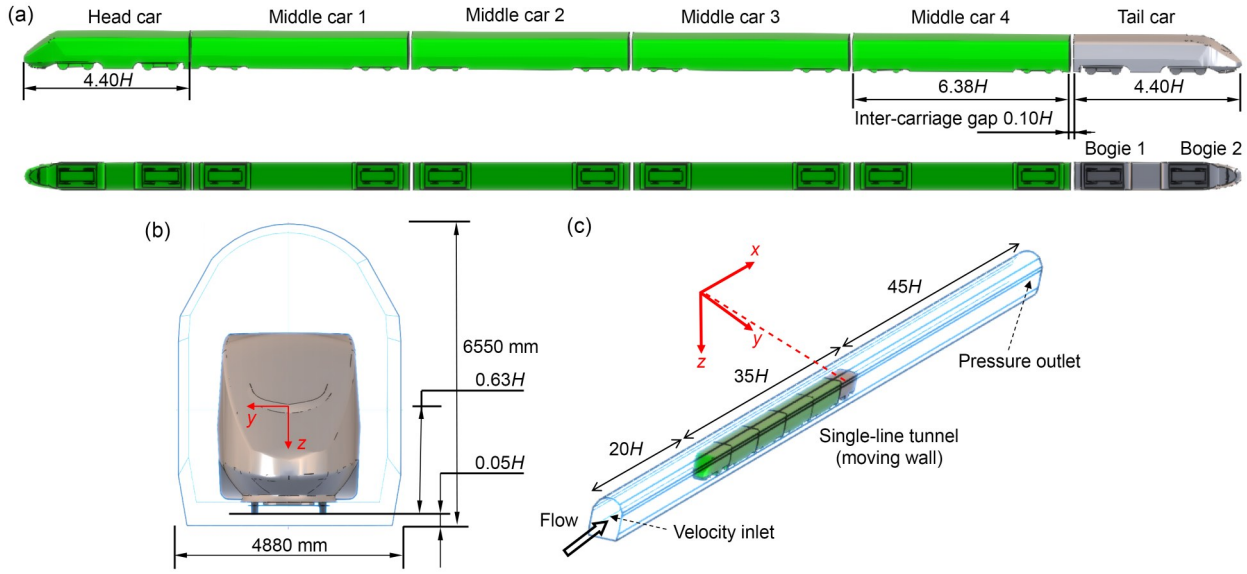

Fig. 5 Train and tunnel aerodynamics model at full scale: (a) side view and bottom view; (b) elevation view; (c) domain and boundaries of computation

3.2 Analysis of aerodynamic performance

According to a recent study by Song et al. (2023), the time-frequency variations of aerodynamic moments M_x and M_z and force F_y acting on a tail car body are almost the same, and are dominated by the vortex-induced frequency of the train wake. Therefore, we only analyzed the lateral movement P_y of the tail car body and the typical vortex-induced force F_y under three conditions, as shown in Figs. 6 and 7, respectively.

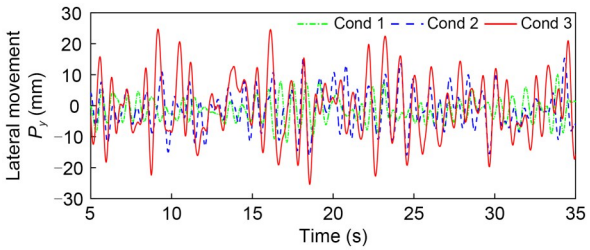

Fig. 6 Lateral movement P_y of the train tail

These figures demonstrate that with increasing lateral movement P_y of the train tail, the vortex-induced force F_y also changes. In Cond 1, when the time-domain amplitude of the train tail P_y is within 10 mm, the dominant frequency of F_y is 1.7 Hz, corresponding to the vortex-induced frequency of the train wake (Schulte-Werning et al., 2003). Furthermore, the vortex-induced frequency is related to tail shape and train speed, which is explained in detail in Sections 4 and 5. As the amplitude of P_y increases, the amplitude of

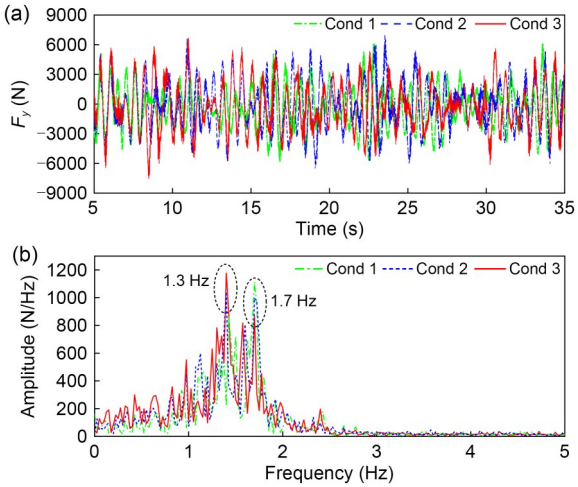

Fig. 7 Vortex-induced force F_y of the train tail: (a) time domain; (b) frequency domain

F_y slightly increases, while its dominant frequency significantly shifts from 1.7 Hz to 1.3 Hz. In Cond 3, when the time-domain amplitude of the train tail P_y increases to 25 mm, the frequency of F_y is dominated by 1.3 Hz, which is the car body hunting frequency at 130 km/h, as verified in Section 3.

In fluid mechanics, the dimensionless frequency St (Strouhal number) is commonly used. It relates the vortex-induced frequency to the flow velocity and characteristic size of the object, and is defined as follows:

$$St = f_{st} \cdot H/U, \tag{2}$$

where f_{st} represents the vortex-induced frequency of the stationary object. In this study, the corresponding f_{st} of the train tail is 1.7 Hz, and the calculated St is about 0.188.

In addition, Suzuki (2004) found that small vibration of the tail car body has little effect on the train wake, while large vibration affects the aerodynamic force, but they did not conduct in-depth research on this subject. Here, for the EMU operating at 130 km/h inside a single-line tunnel, the vortex-induced frequency of the train wake is 1.7 Hz, which approaches 1.3 Hz of the car body hunting frequency. As the swaying amplitude of the train tail increases, the vortex-induced frequency shifts from 1.7 Hz to 1.3 Hz, and the VIV resonance occurs.

3.3 Analysis of wake characteristics

The vortex around the train tail is powerful (with high vorticity), and it falls off in pairs from the tail nose to the downstream, in a similar fashion to the Karman vortex street. As time progresses, the train wake turns into fully developed turbulent vortices. The train wake is an intensive turbulent flow with remarkable unsteadiness, and the aerodynamic force of the tail vehicle is severely affected by the generation, evolution, and collapse of wake vortices (Yao et al., 2013).

Fig. 8 shows the wake vortex structure of the EMU running in a single-line tunnel, as detected from the Q criterion, in which Q is dimensionless and defined as $(U/H)^2$, with values of 0.100, 0.050, 0.010, and 0.001. It can be observed that high-intensity vortices

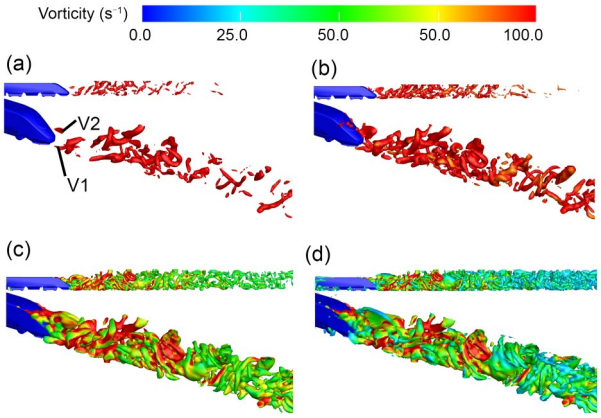

Fig. 8 Wake vortex structures inside the tunnel with various Q values (Cond 2, t=19 s): (a) Q=0.100; (b) Q=0.050; (c) Q=0.010; (d) Q=0.001. References to color refer to the online version of this figure

of the train wake are well captured by the Q criterion. Meanwhile, with higher values of Q, the high-intensity vortices separated from the shear layer of the train-tail surface are more clearly shown, and the low-intensity vortices in the train wake gradually appear. In addition, the initial vortices separated from the tail nose can be divided into two major vortex structures (V1 and V2) on both sides of the train tail; these are described in detail below.

To further illustrate the variation law of the tail aerodynamic force (i.e., vortex-induced force) with train-wake development, we analyzed a complete cycle of the vortex evolution in the train wake under Cond 2. We also obtained the instantaneous vorticity contours at 10 different times located on the vertical section x=0.5H downstream from the nose tip of the train tail, as shown in Fig. 9.

What can be seen from Fig. 9 is that a pair of counter-rotating streamwise vortices alternately appear in the train wake, and with the evolution of the vortex, the aerodynamic force F_y changes periodically. At time 1 and time 2, the clockwise vortex V1 on the left side of the train tail is the most significant, that is, the vortex core with high vorticity appears, and the aerodynamic force reaches its maximum. Subsequently, vortex V1 dissipates, and the aerodynamic force gradually decreases, as shown at time 3. Then, counterclockwise vortex V2 on the right side of the train tail begins to appear, and the aerodynamic force gradually increases in reverse. At time 5 and time 6, when vortex V2 becomes the most significant, the aerodynamic force reaches the reverse maximum. Meanwhile, there is a tendency for the dominant vortex V2 to separate into another reverse vortex V1 on the other side. Through this cycle, the periodic aerodynamic force caused by wake vortex-shedding is formed.

4 Validation

4.1 On-track tests

The real-time aerodynamic force acting on the car body during train operation is difficult to measure, unlike the acceleration response of the car body under aerodynamic force. In order to obtain the vibration characteristics of the train tail inside a single-line tunnel, our study team conducted on-track tests on the Yuxi-Mengzi line of Yunnan, China, in Nov. 2022.

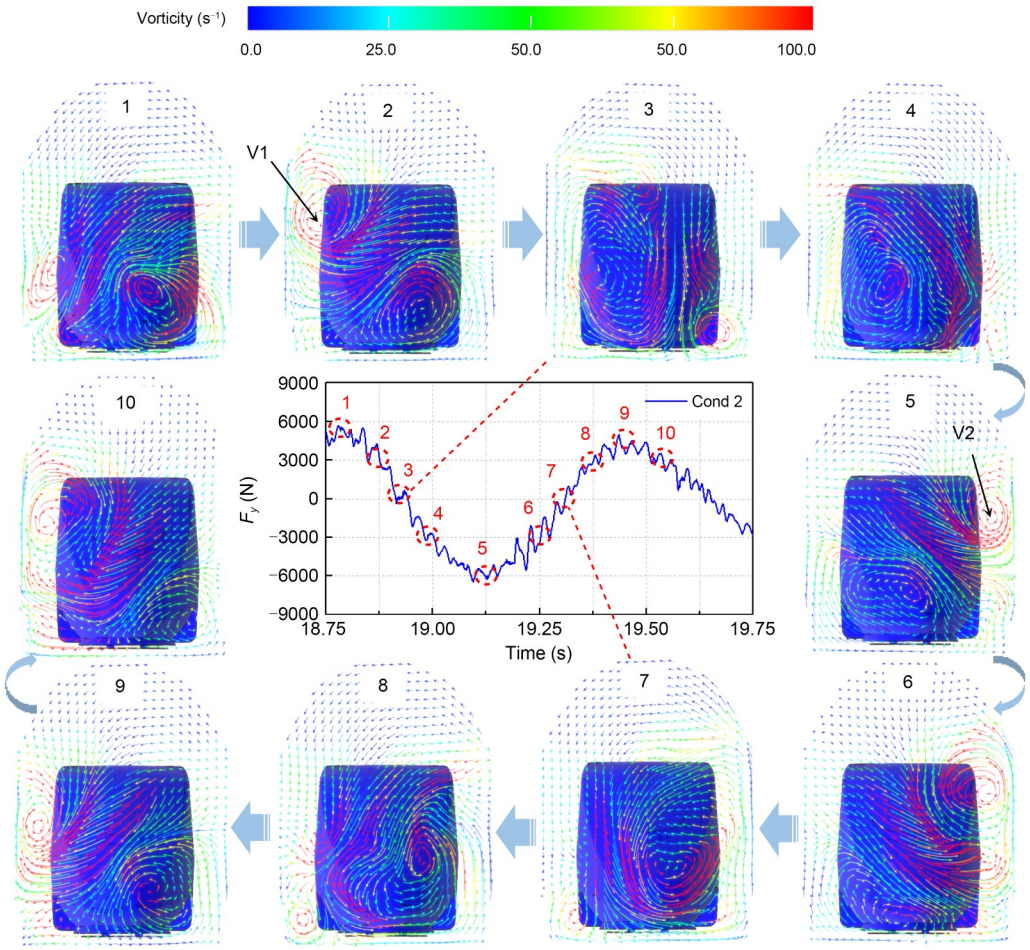

Fig. 9 Cycle of the vortex evolution in the train wake (Cond 2, x=0.5H). References to color refer to the online version of this figure

In the tests, the train speed was approximately 130 km/h. As shown in Fig. 10b, the vibration of the EMU tail was analyzed, and a car body vibration acceleration sensor was placed on the rear cab of the train tail. As in GB/T 5599-2019 (NRA, 2019), we used the lateral ride index W_y calculated by the car body acceleration. The W_y value of less than 2.75 indicates excellent lateral ride comfort for a motor vehicle, as illustrated in Table S1 of the ESM.

Fig. 11 shows the lateral vibration results for the train entering a single-line tunnel at 130 km/h. It can be seen that in the open section, the acceleration of the train tail was within 0.05g (g is the acceleration of gravity), and the W_y was less than 2.75. After entering the tunnel, the lateral vibration acceleration of the train tail rapidly increased to an amplitude of about 0.12g, and ride comfort deteriorated sharply, with a maximum W_y of 3.30.

Next, we conducted frequency-domain analysis of the car body lateral acceleration. As shown in Fig. 12a, the dominant frequency of the lateral vibration of the train tail was 1.3 Hz in the open section, which represents the car body's hunting frequency at 130 km/h. Furthermore, when the train tail vibrated violently under the aerodynamic force in the tunnel section, the swaying frequency of the train tail remained around 1.3 Hz of its natural frequency, as shown in Fig. 12b.

4.2 Wind-tunnel experiment

Because of the limitations of the full-scale vehicle experiment, we decided to study the aerodynamic characteristics of the train tail through a wind-tunnel experiment on a reduced-scale train model. This experiment was conducted in the Aerodynamics Laboratory of Southwest Jiaotong University, China in May 2023.

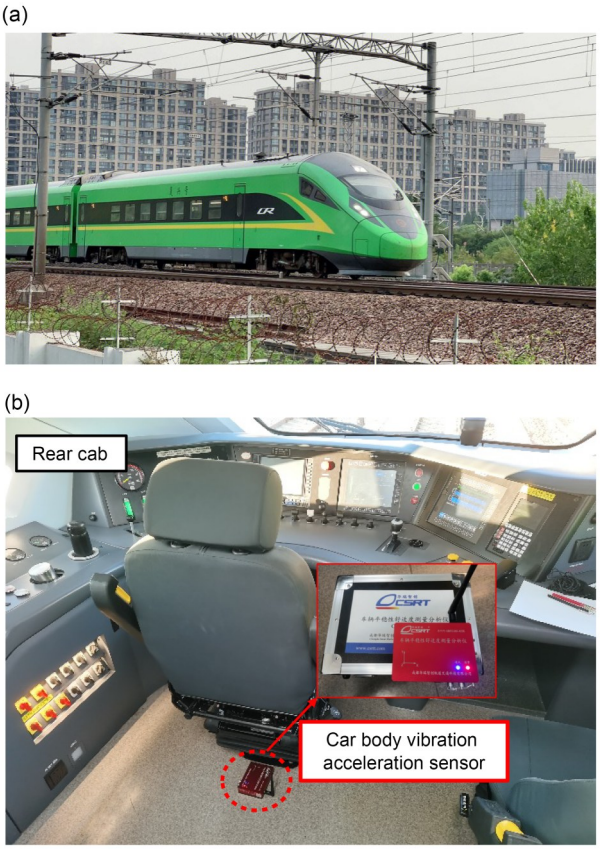

Fig. 10 Tested train: (a) 160 km/h EMU tail; (b) vibration measurement of the EMU tail

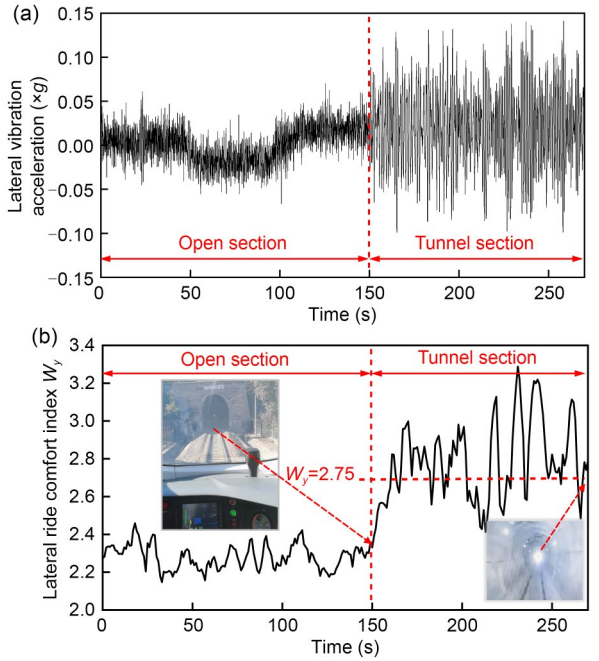

Fig. 11 Test results for a train entering a single-line tunnel: (a) lateral vibration acceleration; (b) lateral ride comfort index

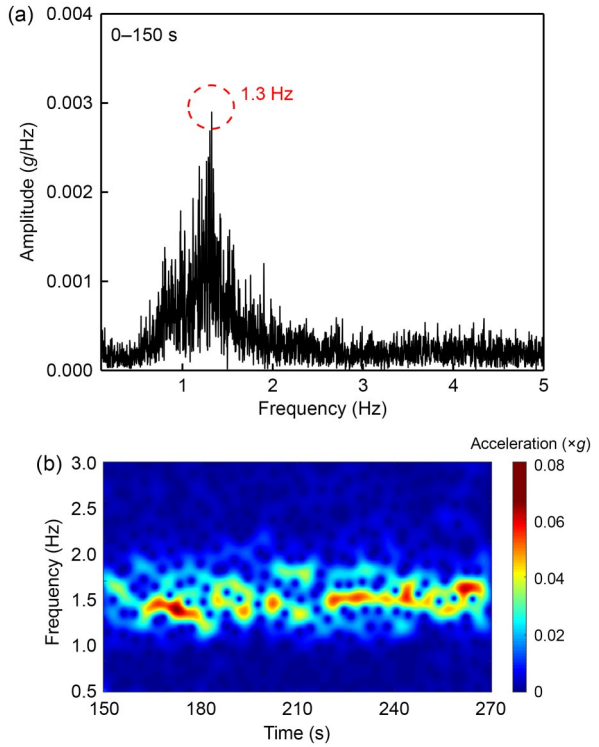

Fig. 12 Frequency-domain analysis of car body lateral acceleration: (a) open section; (b) tunnel section. References to color refer to the online version of this figure

The simplified 1/25 train model of the 160 km/h EMU was based on the wind-tunnel experiment conducted by Hemida and Krajnović (2009), which consisted of a head dummy attached to the tail vehicle, as shown in Fig. 13a. In order to make the airflow generated by the open wind tunnel more uniform around the train and facilitate the measurement of wind speed, a fairing was added around the train model. The train model was made by 3D printing, and the bogie structure was omitted. The length, width, and height of the train model were 1.20 m, 0.13 m, and 0.16 m, respectively, as introduced in detail in the following Section 4.3. In addition, the train head was fixed to rotate around the z-axis, and the train tail could move laterally along the y-axis by spring suspension, as shown in Fig. 13b. An acceleration sensor was also installed at the train tail, and the sampling frequency was 1000 Hz. For the whole vehicle dynamics system, the train-tail swaying phenomenon was mainly reflected in the lateral movement P_y, rolling motion α, and yawing motion γ of the tail car body. However, when carrying out our simplified wind-tunnel experiment, we only considered the lateral movement P_y

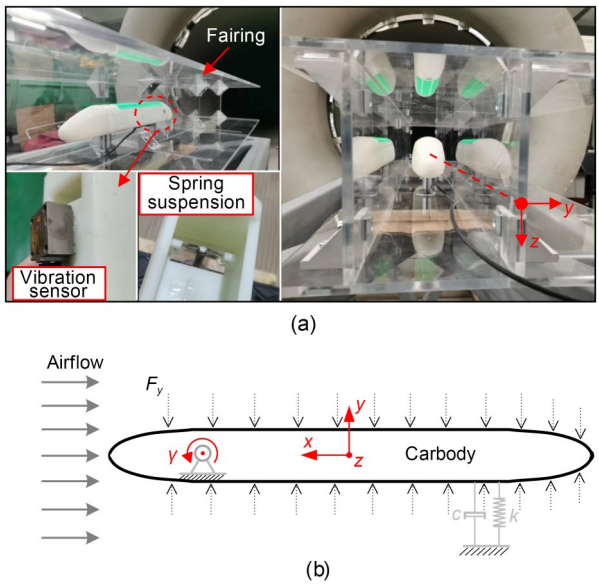

Fig. 13 Train model and wind tunnel: (a) on-site photo; (b) force diagram

of the car body, so the equation for the lateral dynamics of the train model is as follows:

$$m\ddot{y}+c\dot{y}+ky=F_y, \tag{3}$$

where m represents the mass of the train model, which was about 0.2 kg; the measured lateral stiffness k and lateral damping c were 500 N/m and 0.8 N·s/m, respectively, as illustrated in Section S4 of the ESM. These parameters are also used in the simulation in Section 4.3 below.

Fig. 14 shows the results of the wind-tunnel experiment. The lateral vibration of the train tail was analyzed in the time domain and frequency domain, and the wind speed slowly increased from 0 to 40 m/s and then decreased to 0. It can be observed that with the increase in wind speed, the maximum amplitude of the vibration acceleration at the train tail reached about 0.5g. At the same time, the main frequency of the lateral vibration under aerodynamic force is clearly shown to be the natural frequency of 8 Hz of the train model. Therefore, we think that the aerodynamic force frequency is dominated by its natural vibration frequency at this time.

Unfortunately, due to the limitations of the experimental conditions and scale model, on the one hand, the aerodynamic force was not directly measured, and on the other hand, it was impossible to accurately measure the aerodynamic response of the train tail under the smaller amount of sway. Therefore, the wind-tunnel experiment results are used as a reference for the simulation analysis of the reduced-scale train model in the following section.

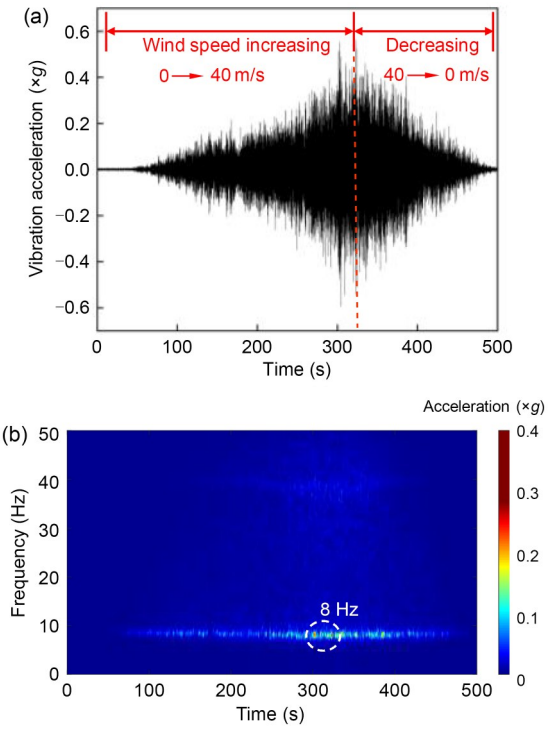

Fig. 14 Lateral acceleration measurement of the train tail: (a) time domain; (b) frequency domain. References to color refer to the online version of this figure

4.3 Train scale-model simulation

4.3.1 Modeling and states

The flow field is large in train aerodynamic calculations, which leads to huge computational demands and low computational efficiency. In order to facilitate our research, we therefore conducted numerical calculations on a reduced-scale train model. The simplified 1/25-scale model of the 160 km/h EMU was based on Hemida and Krajnović (2009), and was composed of a head dummy attached to the tail vehicle, as shown in Fig. 15a.

The aerodynamics model of the smaller train is illustrated in Fig. 15b. The width and height of the computational domain are 20h and 12h, respectively, of which h represents the height of the train scale-model. The height of the train model above the ground is 0.05h, as in (Li L et al., 2022). Moreover, the train is located at a distance of 15h from the inlet

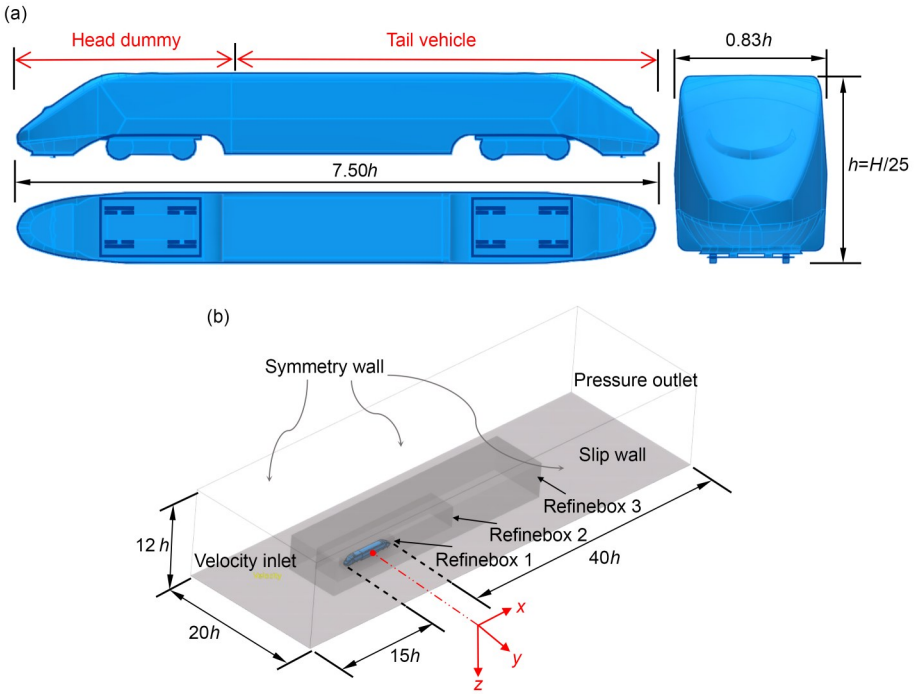

Fig. 15 Aerodynamics model of the 1/25-scale train: (a) simplified model based on the 160 km/h EMU; (b) computational domain and boundary conditions

boundary and 40*h* from the outlet boundary, which meets the requirement of CEN standard (CEN, 2022) that the computational domain should extend at least 8 characteristic heights upstream of the train and at least 16 characteristic heights downstream. Furthermore, the inlet boundary is set to velocity inlet with the incoming airflow velocity *V*, which represents the train speed. The outlet boundary is set to pressure outlet with a reference pressure of 0 Pa. The ground is set as a slip wall, and the slip velocity is the inlet velocity *V*, in order to simulate the relative motion to the train. The top surface and two side surfaces of the computational domain are defined as the symmetry wall. Finally, the surface of the train has the same parameters as the wall model in Section 2.3.

The calculated particle distribution of the computational domain is illustrated in Fig. S4 of the ESM. In addition, the calculation time step is set to 0.05 ms, and the independence verification method is the same as described in Section 2.3. The accuracy of the model was further verified by the consistency of the simulation and experimental results given below.

In order to analyze the aerodynamic influence of the train-tail swaying on the wake flow field, we analyzed the aerodynamic performance of the car body in the following two states: state 1: car body fixed; state 2: lateral rigid-body motion (with mass *m*, stiffness *k*, and damping *c*).

State 2 is completely consistent with the wind-tunnel experiment, and a rigid body with a single lateral degree of freedom was built in Simpack, with a mass *m* of 0.2 kg, stiffness *k* of 500 N/m, and damping *c* of 0.8 N·s/m. The air density was set to 1.205 kg/m^3 at a standard atmospheric pressure of 101.325 kPa and temperature of 20 ℃. The simulation time was 20 s, in which the velocity *V* gradually increased from 0 to 40 m/s in the first 10 s, and then gradually decreased to 0, that is, the velocity changed linearly by 4 m/s.

4.3.2 Results and discussion

Fig. 16 displays the results of aerodynamic lateral force in state 1. It can be seen from Fig. 16a that the vortex-induced frequency of the train wake increases linearly with train speed. When the speed reaches 40 m/s, the corresponding vortex-induced frequency is 48 Hz, so it can be calculated that the vortex-induced frequency f_{st} is about 43 Hz at a train speed of 36 m/s (130 km/h). Meanwhile, the calculated $St=f_{st}\cdot h/V=0.188$ is consistent with the results for

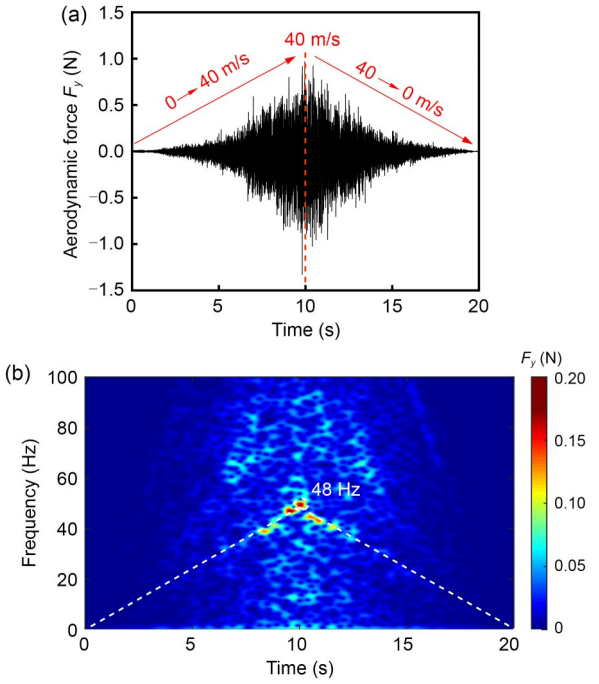

Fig. 16 Aerodynamic lateral force F_y in state 1: (a) time domain; (b) frequency domain. References to color refer to the online version of this figure

the real, full-scale train in Section 2, and the vortex-induced frequency is 43/1.7≈25 times that of the full-scale train, which corresponds to the scale of the model.

Therefore, we can conclude that the vortex-induced frequency of the train wake is only related to the train speed and train-tail nose shape. In addition, with increasing train speed, the vortex-induced frequency increases linearly, while it increases inversely with the scale of the train model.

In addition, when the train speed V reaches 36 m/s, the corresponding Reynolds number is about 3.88×10^5, which is much larger than the critical Reynolds number 2.5×10^5 of CEN standard (CEN, 2022). Therefore, the influence of the Reynolds number on the aerodynamic characteristics of the train can be ignored (Tschepe et al., 2021).

Fig. 17 shows the aerodynamic response of the train tail in state 2, including the lateral vibration acceleration, lateral movement P_y, and aerodynamic lateral force F_y. As shown in Fig. 17a, the lateral acceleration amplitude of the train tail is about 0.5g, which is consistent with the wind-tunnel test results in Fig. 14a. Therefore, the accuracy of the simulation model can be verified. It can be observed from Fig. 17b that the

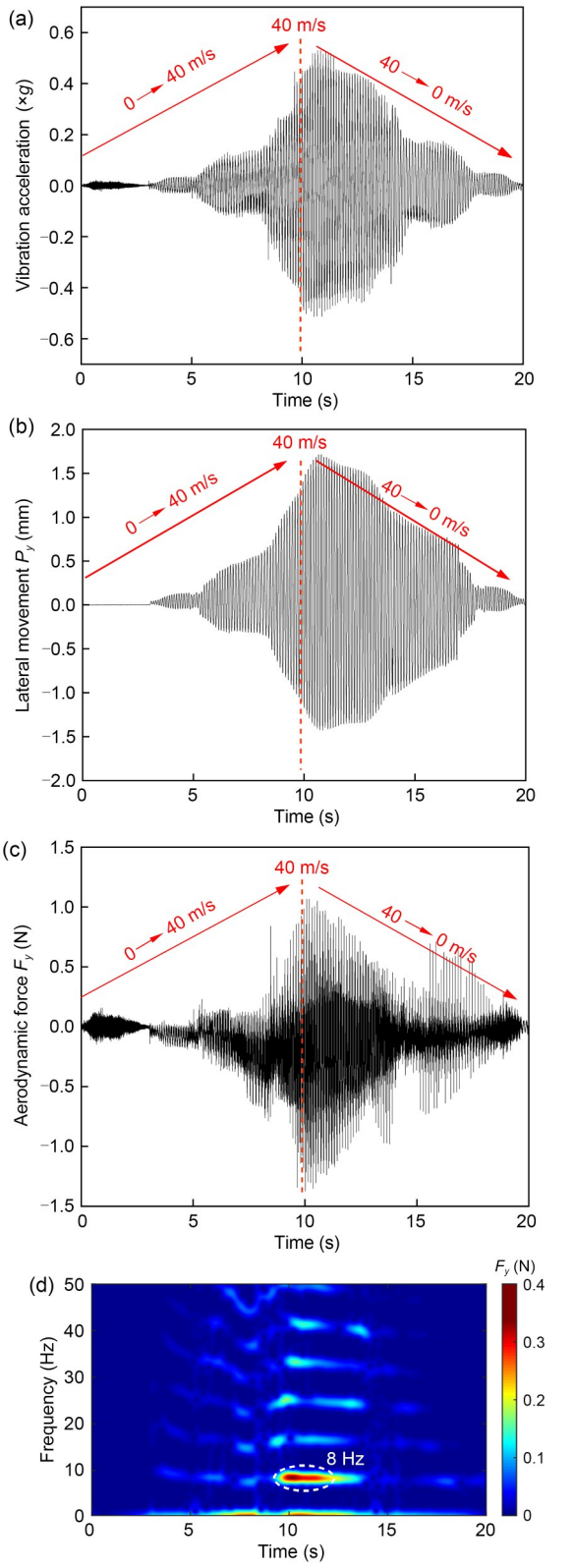

Fig. 17 Aerodynamic responses of the train tail in state 2: (a) lateral vibration acceleration; (b) lateral movement P_y; (c) F_y in time domain; (d) F_y in frequency domain. References to color refer to the online version of this figure

amplitude of P_y is about 1.5 mm, corresponding to the full-scale train (32.5 mm), which is approximately the same as the amplitude of about 25.0 mm of the EMU train tail shown in Fig. 8a, and thus the simulation has certain practical significance as a reference. The time-domain and frequency-domain results of the aerodynamic lateral force F_y are shown in Figs. 17c and 17d, respectively. When the train tail sways laterally with a large amplitude, it is evident that the dominant frequency of F_y is the train's natural frequency of 8 Hz, which indicates the occurrence of frequency-locking. However, the value of F_y is obviously different from that in Fig. 16, and our analysis is that the fluid–structure coupling effect changes the vortex-induced frequency of the train wake.

It is certain that the aerodynamic force is caused by the aerodynamic pressure acting on the surface of the car body, and the aerodynamic pressure distribution on the car body surface will change significantly when the train tail sways. For ease of comparison, the aerodynamic pressure on the car body surface is adjusted to be non-dimensional according to the CEN standards (CEN, 2019, 2022), and the normalized aerodynamic pressure coefficient C_p is defined as follows:

$$C_p = (P - P_\infty)/(0.5\rho_1 V^2), \tag{4}$$

where P is the static pressure; P_∞ is the reference pressure and is equal to 0 Pa; ρ_1 is the air density, which is set to 1.205 kg/m^3 at the standard atmospheric pressure of 101.325 kPa and a temperature of 20 °C. The income airflow velocity V is equal to 40 m/s at 10 s.

The lateral pressure distributions on the train surface in the two states are compared in Fig. 18. The horizontal axis is defined as the dimensionless position L, which represents the distance from the front end of the train. It is clear that when the train sways laterally, the C_p distribution at the front end of the train changes slightly, while the C_p distribution at the train tail changes significantly. Specifically, the prominent point of C_p at the train tail obviously moves downstream to the nose tip, and the variation range ΔP of the aerodynamic pressure coefficient increases.

To further explain the influence of train-tail swaying on the aerodynamic pressure on the train surface, we conducted a comparative analysis of the flow field around the train tail in both states. Fig. 19 shows the

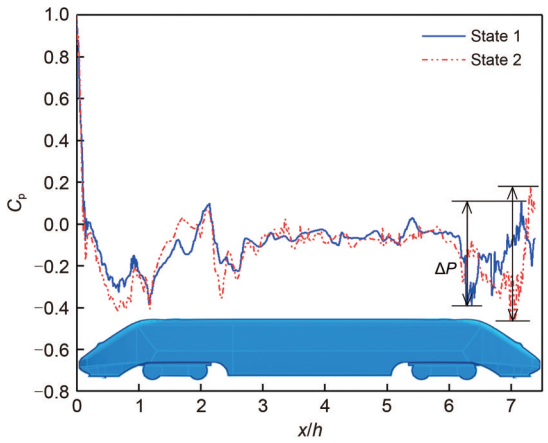

Fig. 18 C_p distribution on the lateral section (t=10 s)

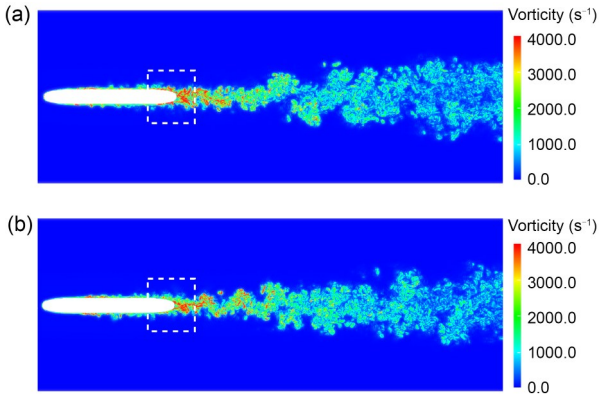

Fig. 19 Contours of the instantaneous vortices in the z-direction at the nose tip of the train tail (t=10 s): (a) state 1; (b) state 2. Reference to color refer to the online version of this figure

instantaneous vorticity contour in the z-direction at the nose tip of the train tail, and the corresponding time t is 10 s, which is consistent with that in Fig. 18 above. It can be observed from Fig. 19 that the vortices detach from the train tail with high intensity, and the vortex intensity gradually decreases as the vortices flow downstream. In state 1, the high-intensity vortex is separated around the tail nose, as indicated by the red box in Fig. 19a. However, in state 2, the separation point of the high-intensity vortex shifts downstream to the nose tip, as indicated by the red box mark in Fig. 19b. This means that when the car body is fixed, the aerodynamic frequency is the vortex-induced frequency related to the tail nose shape (Fig. 16b). When the train tail is swaying severely, the aerodynamic frequency becomes the natural vibration frequency of the train model, which is independent of the aerodynamic shape (Fig. 17d).

In summary, train-tail swaying affects the flow field of the train wake, and the separation point of the thick turbulent boundary layer on the surface of the train tail moves downstream to the nose tip, thereby changing the vortex-induced frequency. For an EMU operating at 130 km/h, the vortex-induced frequency calculated based on its aerodynamic shape is about 1.7 Hz, which approaches the natural frequency of car body hunting of 1.3 Hz. In addition, the aerodynamic effect inside a single-line tunnel is strong (the amplitude of F_y reaches 6 kN), which causes VIV of the train tail. As the lateral movement of the train tail increases, the vortex-induced frequency shifts from 1.7 Hz to 1.3 Hz, and the frequency-locking characteristic of VIV appears, with the resonance causing the train tail to sway continuously in the single-line tunnel.

5 Countermeasures

We pinpointed two fundamental reasons for the continuous train-tail swaying of a 160 km/h EMU in a single-line tunnel, through early vehicle development and later experimental research conducted by our research team: First, for the motor vehicle of the train tail, its own primary hunting stability (i.e., car body hunting) is not enough. Second, the aerodynamic effect in a single-line tunnel is strong, and the periodic vortex-induced force of the train wake leads to VIV of the train tail, which causes a resonance of the tail car body.

In this section, we put forward two main countermeasures for train-tail swaying in single-line tunnels. One is to improve its primary hunting stability through vehicle suspension, and the other is to reduce the aerodynamic vortex shedding force of the train tail by optimizing the aerodynamic shape.

5.1 Optimization of vehicle suspension

Train-tail swaying is part of the car body hunting motion, which is also called primary hunting motion in the field of railway vehicle dynamics. According to the theory of railway vehicle suspension (Iwnicki et al., 2020), reducing the secondary suspension damping of a vehicle system to within a certain range is beneficial in improving its primary hunting stability. Therefore, we propose improvement 1, which involves reducing the yaw-damper damping C_{sx} from the normal 800 kN·s/m to 600 kN·s/m.

In addition, the installation arrangement of the yaw damper is generally divided into two types, called opening outward (OO) and skew symmetry (SS), as illustrated in Fig. S5 of the ESM. The 160 km/h EMU tail car body has an SS yaw-damper arrangement, and there is no doubt that the SS arrangement improves the dynamic performance of the car body in some ways. However, as shown in Table 1, when the train operates on the open section (without F_y), the W_y of the front end of the car body is 2.08, while the W_y of the rear end is 2.34, indicating that the lateral ride comfort of its rear end is relatively poor; this has been confirmed by Li G et al. (2022, 2023a) and Song et al. (2023). According to the research of Li et al. (2023b), the OO arrangement is beneficial in reducing the lateral ride index difference between the two ends of the car. Therefore, we propose improvement 2, changing the arrangement of the yaw damper from the normal SS to OO.

The dynamic performances of the tail car with improvements 1 and 2 are shown in Table 1, in which the calculation condition is Cond 2 (shown in Section 3.1). It can be observed that the W_y of the tail car is 2.34 in the open section (without F_y), but deteriorates to 2.90 in the single-line tunnel (with F_y), which is consistent with the results from the on-track tests (Fig. 11b). In addition, we measured the W_y of the train tail with each improvement separately, and found that with improvements 1 and 2, the W_y of the train tail is 2.74 and 2.72, respectively, both of which are at the excellent level (less than 2.75), indicating that these two improvements to the yaw damper can effectively alleviate the train-tail swaying in a single-line tunnel.

Table 1 Vehicle dynamic performance (without/with aerodynamic force F_y)

Vehicle suspension	Yaw damper damping C_{sx} (kN·s/m)	Yaw damper arrangement	Lateral ride comfort W_y	
			Front-end	Rear-end
Normal	800	SS	2.08/2.13	2.34/2.90
Improvement 1	600	SS	2.05/2.11	2.26/2.74
Improvement 2	800	OO	2.14/2.17	2.15/2.72

5.2 Optimization of aerodynamic shape

A good streamlined car body shape is beneficial in reducing aerodynamic resistance during train operation. Because of the vortex-shedding characteristics of the train wake, the high-intensity vortices mainly detach from the tail nose. Therefore, on the basis of the original car body shape, we only changed the aerodynamic shape of the tail nose and extended it by 0.4H along the x-axis, as shown in Fig. 20.

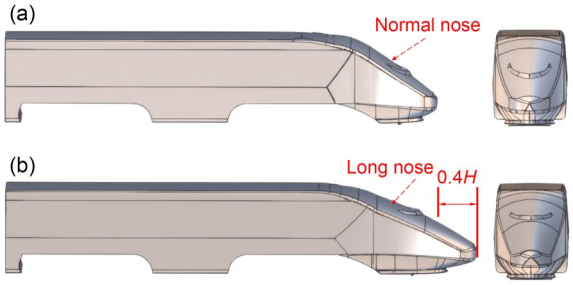

Fig. 20 Aerodynamic optimization of the train-tail nose shape: (a) normal nose; (b) long nose

Fig. 21 shows the aerodynamic vortex-induced force F_y of the train tail with two different nose shapes under calculation conditions Cond 2. The F_y amplitude of the long-nose train is about 5 kN, and the vortex-induced frequency is 1.1 Hz. In addition, compared with the normal short-nose train, the W_y of the train tail of the long-nose car body is reduced from 2.90 to 2.65.

Referring to the research by Hemida et al. (2009, 2014), we found that the wake of the short-nose train shows more high-intensity vortex structures than that of the long-nose train. We believe that compared with the short-nose vehicle, the long-nose train reduces the amplitude of the aerodynamic vortex-induced force of the train tail, and also decreases the vortex-induced frequency.

For an EMU operating at 130 km/h, the long-nose car body will cause the decrease in the vortex-induced frequency from 1.7 Hz to 1.1 Hz, although it is closer to the car body hunting frequency of 1.3 Hz. However, the amplitude of the aerodynamic vortex-induced force F_y will be reduced from 6 kN to 5 kN (17%), thus greatly weakening the aerodynamic effect and improving the lateral ride comfort of the train tail running in a single-line tunnel.

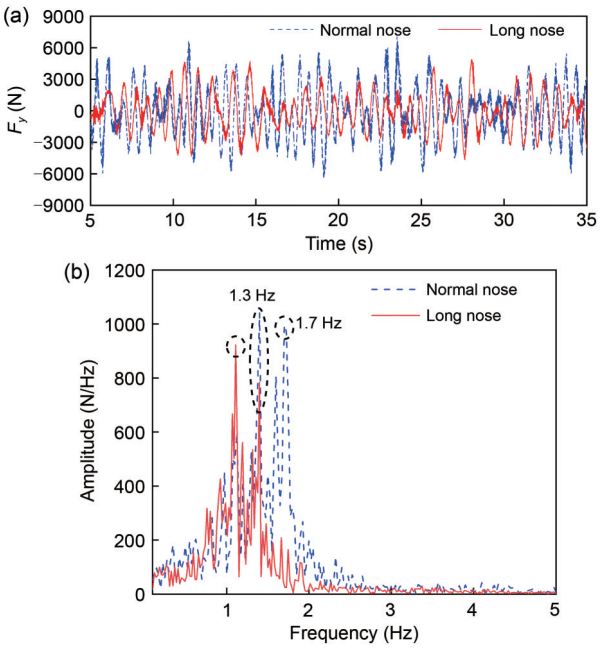

Fig. 21 Aerodynamic vortex-induced force F_y of the train tail under Cond 2: (a) time domain; (b) frequency domain

6 Conclusions

Aiming to improve the train-tail swaying of 160 km/h EMUs in single-line tunnels, which is an urgent on-site problem, we studied the aerodynamic performance of the train tail through experiments and simulations. The influence mechanism of train-tail swaying on train-wake characteristics was revealed. This permitted us to suggest countermeasures for train-tail swaying in single-line tunnels, with regard to two key aspects. The major conclusions of this study are as follows:

(1) When the train tail sways with a small amplitude (within 10 mm), its aerodynamic force frequency (i.e., vortex-induced frequency) is about 1.7 Hz at 130 km/h, which is related to the train speed and the nose shape of the train tail. At higher train speeds, the vortex-induced frequency of the train wake increases linearly. In addition, when the tail nose is extended, the vortex-induced frequency decreases.

(2) As the swaying amplitude of the train tail increases (exceeding 25 mm), the separation point of the high-intensity vortex in the train wake shifts downstream to the nose tip, thereby changing the vortex-induced frequency from 1.7 Hz to the nearby car body hunting frequency of 1.3 Hz. This suggests that the

frequency-locking characteristic appears, and the resonance caused by VIV intensifies train-tail swaying.

(3) For the motor vehicle of the train tail, adopting an OO arrangement for the yaw damper or reducing yaw-damper damping within a certain range can effectively weaken train-tail swaying inside single-line tunnels. In addition, when the tail nose is extended, the amplitude of the vortex-induced force is reduced, thereby weakening the aerodynamic effect and effectively alleviating the train-tail swaying inside single-line tunnels.

Acknowledgments

This work is supported by the National Natural Science Foundation of China (Nos. 52372403 and U2268211), the Natural Science Foundation of Sichuan Province (No. 2022NSFSC0034), China, the National Railway Group Science and Technology Program (No. 2023J071), and the Traction Power State Key Laboratory of the Independent Research and Development Projects (No. 2022TPL-T02), China.

Author contributions

Yadong SONG wrote the first draft of the manuscript. Yadong SONG and Longjiang SHEN processed the corresponding data. Yanpeng ZOU and Ting QIN helped to organize the manuscript. Yuan YAO designed the research, and revised and edited the final version.

Conflict of interest

Yadong SONG, Yanpeng ZOU, Yuan YAO, Ting QIN, and Longjiang SHEN declare that they have no conflict of interest.

References

Bell JR, Burton D, Thompson M, et al., 2014. Wind tunnel analysis of the slipstream and wake of a high-speed train. *Journal of Wind Engineering and Industrial Aerodynamics*, 134:122-138. https://doi.org/10.1016/j.jweia.2014.09.004

Bell JR, Burton D, Thompson MC, et al., 2015. Moving model analysis of the slipstream and wake of a high-speed train. *Journal of Wind Engineering and Industrial Aerodynamics*, 136:127-137. https://doi.org/10.1016/j.jweia.2014.09.007

Bell JR, Burton D, Thompson MC, et al., 2016a. Flow topology and unsteady features of the wake of a generic high-speed train. *Journal of Fluids and Structures*, 61:168-183. https://doi.org/10.1016/j.jfluidstructs.2015.11.009

Bell JR, Burton D, Thompson MC, et al., 2016b. Dynamics of trailing vortices in the wake of a generic high-speed train. *Journal of Fluids and Structures*, 65:238-256. https://doi.org/10.1016/j.jfluidstructs.2016.06.003

CEN (Comité Européen de Normalisation), 2019. Railway Applications-Aerodynamics-Part 4: Requirements and Test Procedures for Aerodynamics on Open Track, EN 14067-4. CEN, Brussels, Belgium.

CEN (Comité Européen de Normalisation), 2022. Railway Applications-Aerodynamics-Part 6: Requirements and Test Procedures for Cross Wind Assessment, EN 14067-6. CEN, Brussels, Belgium.

Choi JK, Kim KH, 2014. Effects of nose shape and tunnel cross-sectional area on aerodynamic drag of train traveling in tunnels. *Tunnelling and Underground Space Technology*, 41:62-73. https://doi.org/10.1016/j.tust.2013.11.012

Diedrichs B, Berg M, Stichel S, et al., 2007. Vehicle dynamics of a high-speed passenger car due to aerodynamics inside tunnels. *Proceedings of the Institution of Mechanical Engineers, Part F: Journal of Rail and Rapid Transit*, 221(4):527-545. https://doi.org/10.1243/09544097JRRT125

Diedrichs B, Krajnović S, Berg M, 2008. On the aerodynamics of car body vibrations of high-speed trains cruising inside tunnels. *Engineering Applications of Computational Fluid Mechanics*, 2(1):51-75. https://doi.org/10.1080/19942060.2008.11015211

Du JM, Fang Q, Wang G, et al., 2022. Aerodynamic effects produced by a high-speed train traveling through a tunnel considering different car numbers. *Symmetry*, 14(3):479. https://doi.org/10.3390/sym14030479

Fujimoto H, Miyamoto M, Shimamoto Y, 1993. Lateral vibration and its decreasing measure in the tail car of a Shinkansen. *Transactions of the Japan Society of Mechanical Engineers Series C*, 59(560):1016-1022 (in Japanese). https://doi.org/10.1299/kikaic.59.1016

Han P, de Langre E, Thompson MC, et al., 2023. Vortex-induced vibration forever even with high structural damping. *Journal of Fluid Mechanics*, 962:A13. https://doi.org/10.1017/jfm.2023.268

Hemida H, Krajnović S, 2008. LES study of the influence of a train-nose shape on the flow structures under cross-wind conditions. *Journal of Fluids Engineering*, 130(9):091101. https://doi.org/10.1115/1.2953228

Hemida H, Krajnović S, 2009. Exploring flow structures around a simplified ICE2 train subjected to a 30° side wind using LES. *Engineering Applications of Computational Fluid Mechanics*, 3(1):28-41. https://doi.org/10.1080/19942060.2009.11015252

Hemida H, Baker C, Gao GJ, 2014. The calculation of train slipstreams using large-eddy simulation. *Proceedings of the Institution of Mechanical Engineers, Part F: Journal of Rail and Rapid Transit*, 228(1):25-36. https://doi.org/10.1177/095440971246098

Iwnicki S, Spiryagin M, Cole C, et al., 2020. Handbook of Railway Vehicle Dynamics. 2nd Edition. CRC Press, Boca Raton, USA. https://doi.org/10.1201/9780429469398

Khier W, Breuer M, Durst F, 2000. Flow structure around trains under side wind conditions: a numerical study. *Computers & Fluids*, 29(2):179-195. https://doi.org/10.1016/S0045-7930(99)00008-0

Li G, Wu RD, Deng XX, et al., 2022. Suspension parameters matching of high-speed locomotive based on stability/comfort Pareto optimization. *Vehicle System Dynamics*, 60(11):3848-3867. https://doi.org/10.1080/00423114.2021.1979602

Li G, Zhou Y, Yao Y, et al., 2023a. Application of yaw dampers with frequency-selective damping to improve the locomotive adaptability to low/high conicity stability. *Proceedings of the Institution of Mechanical Engineers, Part F: Journal of Rail and Rapid Transit*, 237(6):784-795. https://doi.org/10.1177/09544097221141517

Li G, Yao Y, Shen LJ, et al., 2023b. Influence of yaw damper layouts on locomotive lateral dynamics performance: Pareto optimization and parameter analysis. *Journal of Zhejiang University-SCIENCE A (Applied Physics & Engineering)*, 24(5):450-464. https://doi.org/10.1631/jzus.A2200374

Li JY, Liu LY, Kou DH, 2014. Wu Guang high-speed rail track irregularity power spectrum analysis. *Applied Mechanics and Materials*, 638-640:1224-1228. https://doi.org/10.4028/www.scientific.net/AMM.638-640.1224

Li L, Liu TH, Guo ZJ, et al., 2022. On the effect of rail-end slope in train aerodynamics under crosswind. *Vehicle System Dynamics*, 60(6):1888-1908. https://doi.org/10.1080/00423114.2021.1883067

Li T, Dai ZY, Yu MG, et al., 2021. Numerical investigation on the aerodynamic resistances of double-unit trains with different gap lengths. *Engineering Applications of Computational Fluid Mechanics*, 15(1):549-560. https://doi.org/10.1080/19942060.2021.1895321

Li T, Liang H, Zhang J, et al., 2023. Numerical study on aerodynamic resistance reduction of high-speed train using vortex generator. *Engineering Applications of Computational Fluid Mechanics*, 17(1):e2153925. https://doi.org/10.1080/19942060.2022.2153925

Li W, Guan QH, Chi MR, et al., 2022. An investigation into the influence of wheel-rail contact relationships on the car body hunting stability of an electric locomotive. *Proceedings of the Institution of Mechanical Engineers, Part F: Journal of Rail and Rapid Transit*, 236(10):1198-1209. https://doi.org/10.1177/0954409722108441

Liu DJ, Li XZ, Mei FL, et al., 2023. Effect of vertical vortex-induced vibration of bridge on railway vehicle's running performance. *Vehicle System Dynamics*, 61(5):1432-1447. https://doi.org/10.1080/00423114.2022.2084120

Niu JQ, Liang XF, Zhou D, 2016. Experimental study on the effect of Reynolds number on aerodynamic performance of high-speed train with and without yaw angle. *Journal of Wind Engineering and Industrial Aerodynamics*, 157:36-46. https://doi.org/10.1016/j.jweia.2016.08.007

Niu JQ, Zhou D, Liu TH, et al., 2017. Numerical simulation of aerodynamic performance of a couple multiple units high-speed train. *Vehicle System Dynamics*, 55(5):681-703. https://doi.org/10.1080/00423114.2016.1277769

Niu JQ, Zhou D, Liang XF, et al., 2018. Numerical simulation of the Reynolds number effect on the aerodynamic pressure in tunnels. *Journal of Wind Engineering and Industrial Aerodynamics*, 173:187-198. https://doi.org/10.1016/j.jweia.2017.12.013

Pan YC, Yao JW, Liu T, et al., 2018. Discussion on the wake vortex structure of a high speed train by vortex identification methods. *Chinese Journal of Theoretical and Applied Mechanics*, 50(3):667-676 (in Chinese). https://doi.org/10.6052/0459-1879-17-383

Schulte-Werning B, Heine C, Matschke G, 2003. Unsteady wake flow characteristics of high-speed trains. *Proceedings in Applied Mathematics and Mechanics*, 2(1):332-333. https://doi.org/10.1002/pamm.200310150

Shi YX, Dai HY, Wang QS, et al., 2020. Research on low-frequency swaying mechanism of metro vehicles based on wheel-rail relationship. *Shock and Vibration*, 2020:8878020. https://doi.org/10.1155/2020/8878020

SIMULIA Inc., 2021. SIMULIA Xflow User's Guide, Release 2021x. SIMULIA Inc., Michigan, USA.

Song YD, Qin T, Yao Y, et al., 2023. Investigation on aerodynamic fluid-structure coupling vibration of 160 km/h EMU tail in single-track tunnels. *International Journal of Structural Stability and Dynamics*, 24(18):2450197. https://doi.org/10.1142/S0219455424501979

NRA (National Railway Administration of the People's Republic of China), 2019. Specification for Dynamics Performance Assessment and Testing Verification of Rolling Stock, GB/T 5599–2019. National Standards of the People's Republic of China (in Chinese).

NRA (National Railway Administration of the People's Republic of China), 2020. Gauge for Standard Gauge Railways-Part 2: Structure Gauge, GB 146.2–2020. National Standards of the People's Republic of China (in Chinese).

Sun JF, Chi MR, Jin XS, et al., 2021. Experimental and numerical study on car body hunting of electric locomotive induced by low wheel-rail contact conicity. *Vehicle System Dynamics*, 59(2):203-223. https://doi.org/10.1080/00423114.2019.1674344

Suzuki M, 2000. Aerodynamic force acting on train in tunnel. *RTRI Report*, 14(9):37-42 (in Japanese).

Suzuki M, 2001. Unsteady aerodynamic force acting on high speed trains in tunnel. *Quarterly Report of RTRI*, 42(2):89-93. https://doi.org/10.2219/rtriqr.42.89

Suzuki M, 2004. Flow-induced vibration of high-speed trains in tunnels. The Aerodynamics of Heavy Vehicles: Trucks, Buses, and Trains, p.443-452. https://doi.org/10.1007/978-3-540-44419-0_39

Takai H, 1990. Maintenance of track with long-wave track irregularity on Shinkansen. *Railway Technical Research Institute, Quarterly Reports*, 31(3):128-131. https://trid.trb.org/view/352202

Tanifuji K, Sakanoue K, Kikko S, 2008. Modelling of aerodynamic force acting on high speed train in tunnel and a measure to improve the riding comfort utilising restriction between cars. *Vehicle System Dynamics*, 46(S1):1065-1075.

https://doi.org/10.1080/00423110802158747

Tschepe J, Nayeri CN, Paschereit CO, 2021. On the influence of Reynolds number and ground conditions on the scaling of the aerodynamic drag of trains. *Journal of Wind Engineering and Industrial Aerodynamics*, 213:104594. https://doi.org/10.1016/j.jweia.2021.104594

Wang JC, Ling L, Ding X, et al., 2022. The influence of aerodynamic loads on car body low-frequency hunting of high-speed trains. *International Journal of Structural Stability and Dynamics*, 22(13):2250145. https://doi.org/10.1142/S0219455422501450

Williamson CHK, Govardhan R, 2004. Vortex-induced vibrations. *Annual Review of Fluid Mechanics*, 36:413-455. https://doi.org/10.1146/annurev.fluid.36.050802.122128

Yao SB, Sun ZX, Guo DL, et al., 2013. Numerical study on wake characteristics of high-speed trains. *Acta Mechanica Sinica*, 29(6):811-822. https://doi.org/10.1007/s10409-013-0077-3

Yao Y, Xu ZF, Song YD, et al., 2021. Mechanism of train tail lateral sway of EMUs in tunnel based on vortex-induced vibration. *Journal of Traffic and Transportation Engineering*, 21(5):114-124 (in Chinese). https://doi.org/10.19818/j.cnki.1671-1637.2021.05.010

Yu HY, Øiseth O, Zhang MJ, et al., 2023. Tuned mass damper design for vortex-induced vibration control of a bridge: influence of vortex-induced force model. *Journal of Bridge Engineering*, 28(5):04023021. https://doi.org/10.1061/JBENF2.BEENG-5958

Zeng XH, Wu H, Lai J, et al., 2014. Influences of aerodynamic loads on hunting stability of high-speed railway vehicles and parameter studies. *Acta Mechanica Sinica*, 30(6):889-900. https://doi.org/10.1007/s10409-014-0119-5

Zeng XH, Lai J, Wu H, 2018. Hunting stability of high-speed railway vehicles under steady aerodynamic loads. *International Journal of Structural Stability and Dynamics*, 18(7):1850093. https://doi.org/10.1142/S0219455418500931

Zhang GQ, Xu YL, Wang B, et al., 2023. Turbulence effects on vortex-induced dynamic response of a twin-box bridge and ride comfort of the vehicle. *International Journal of Structural Stability and Dynamics*, 23(16n18):2340023. https://doi.org/10.1142/S0219455423400230

Zhao X, Tan M, Zhu WD, et al., 2023. Study of vortex-induced vibration of a pipe-in-pipe system by using a wake oscillator model. *Journal of Environmental Engineering*, 149(4):04023007. https://doi.org/10.1061/JOEEDU.EEENG-7178

Zhou L, Ge YJ, 2008. Wind tunnel test for vortex-induced vibration of vehicle-bridge system section model. *Journal of the Brazilian Society of Mechanical Sciences and Engineering*, 30(2):110-117. https://doi.org/10.1590/S1678-58782008000200003

Electronic supplementary materials

Sections S1–S6, Table S1, Figs. S1–S5